

A Novel Triad Twisted String Actuator for Controlling a Two Degrees of Freedom Joint: Design and Experimental Validation

Damian Crosby, Joaquin Carrasco *Member, IEEE*, William Heath *Member, IEEE*, and Andrew Weightman

Abstract—Actuated universal joints, or equivalent joint systems, are found in a number of robotic applications, in particular mobile snake robots, snake-arm robots and robotic tails. Such joints use a variety of actuation methods, including direct drive motors, linear screw drives, cable based systems, and hydraulics/pneumatics. In this paper the authors present a novel design for a mechanism that utilises the twisted string actuator in an antagonistic triad to actuate the universal joint, using orientation sensors and load cells to create a robust cascading closed loop control system. This design realises a light, compact, high-performance actuation system that avoids the extra mass and hardware complexity that alternative actuation methods present, with the additional challenge of nonlinearity. The authors were able to develop a closed loop control system that could track a universal joint orientation setpoint to within $\pm 1.8^\circ$ within a $\pm 11^\circ$ range for a single axis and $\pm 6^\circ$ range for dual axis.

Index Terms—???

I. INTRODUCTION

Actuated universal joint (AUJ) mechanisms are found in a wide range of robotic applications, such as confined space inspection using continuum robots [1], highly manoeuvrable mobile snake robots [2], and biomimetic robot tails for stability [3]. Mobile snake robots must usually incorporate electric actuators inline with their joints. This results in an AUJ having to shift the mass of the follower segments and all the actuators inside the follower segments, which results in high torque requirements. Continuum robots and robotic tails can reduce the mass and size of the AUJ by moving their actuators away from the AUJs and use cables to transfer the force to the joints, or use hydraulic or pneumatic actuators which tend to be lighter than equivalent electric motors. This comes at the expense of increased mass and bulk at the base of the arm or tail.

First developed by Würtz *et al.* [4] in 2010, the TSA uses two or more strings between two fixtures as a linear

D. Crosby, and A. Weightman are with the Department of Mechanical, Aerospace and Civil Engineering, School of Engineering, Faculty of Science and Engineering, The University of Manchester, Manchester, United Kingdom.

J. Carrasco and W. Heath are with the Department of Electrical and Electronic Engineering, School of Engineering, Faculty of Science and Engineering, The University of Manchester, Manchester, United Kingdom.

actuator. When one fixture is rotated (typically by an electric motor), the looped string twists into a helix, decreasing the distance between them. TSA actuators have been used for a hand orthosis [5], elbow joint [6] and foldable robot arm [7] among other functions.

The primary advantage of TSA over similar linear actuators such as a leadscrew is the reduction (lower velocity, higher torque) the TSA provides is not proportional to the mass of the actuator, in fact it is slightly inversely proportional. Generally, to increase the reduction in an actuator requires the addition of a gearbox which increases mass, but in the case of the TSA, by decreasing the string cross-section radius, the reduction increases given a constant unwound length and motor angle, resulting in a greater reduction with no increase, or even a slight decrease, in actuator mass.

While the reduction in a leadscrew can be increased by decreasing the lead on the thread, which also has no increase in mass, this has a limited range and can quickly run up against manufacturing tolerances or material strength requirements. In order to achieve greater or more robust reductions, the screw radius has to be increased, or the driving motor has to have a larger reduction before driving the screw, both of which usually result in more material (typically steel) and therefore more mass.

However, TSA does have some disadvantages, the most significant of which is a nonlinear reduction equation, which is also dependent on the motor angle (and therefore actuator position). The reduction decreases in a nonlinear fashion as the angle increases, with the derivative decreasing as the angle increases. There is also the compliance of the strings to consider, depending on the thickness and material chosen, which becomes a significant factor under high forces. Both of these issues can be addressed with accurate modelling [8] and/or a robust control strategy, as demonstrated in [4]. What is more of an issue is the unidirectional force of the TSA, which can only impart force in tension. This means that for an AUJ, which is a 2 degree of freedom (DOF) joint, a minimum of three TSA are required, unless spring return mechanisms are used, which would impart additional force on the TSA and therefore reduce performance. However, the potential high force to mass ratio of the TSA due to the non-proportional reduction may adequately compensate for the additional

actuator requirement.

The focus of this research is to investigate if the TSA is a suitable candidate for control of an AUJ considering both the benefits and drawbacks. To this end, the objective is to simulate a model and then construct a physical experimental prototype to validate the proposed control system.

The use of TSA as an actuator for an AUJ is an understudied area of research. Bombara, Konda, Chow, *et al.* [9] have proposed a similar design using a flexible core with continuous curvature as opposed to a rigid universal joint, however currently this research has not demonstrated control of both axes of motion with multiple TSA. For the first time the authors demonstrate a robust closed loop control of an AUJ in both axes of motion using three TSA in an “antagonistic triad” configuration. The result is a light, compact AUJ design that has the potential to significantly improve upon exiting inline actuation options.

This publication will first give an outline of the TSA based on the existing literature, and the concept of an antagonistic triad. Then a detailed explanation of the control system is given, followed by results from the simulation and experimental system. Finally, a theoretical analysis of the TSA AUJ compared to a similar AUJ using leadscrews is conducted, followed by a discussion and conclusion.

This work was previously published as a conference proceeding at the International Conference on Robotics and Automation (ICRA) 2022 [10]. This publication extends that research by including additional experimental results with increased follow mass and joint velocity, as well as adjusting a parameter in the control system to increase the joint range. It also details additional preliminary work that was done to characterise each individual TSA under force control, including exploration of alternative TSA inner loop control systems. Finally, it adds additional content to the discussion and proposes further improvements to the design for future work.

A. A Twisted string actuator

First developed by Würtz, May, Holz, *et al.* [4] in 2010, TSA uses two or more strings between two fixtures as a 1 DOF linear actuator. When one fixture is rotated (typically by an electric motor), the strings twist into a helix, decreasing the distance between the fixtures, as shown in figure 1. Given the unwound length l_u , and the cross-section radius of the string r_s (or $r_s + r_c$ when there are more than two strings) as shown in figure 2, the actuator length is given by

$$l_s(\theta_s) = \sqrt{l_u^2 - \theta_s^2 r_s^2} \quad (1)$$

where θ_s is the motor angle, as shown in figure 3.

This equation assumes an infinite string stiffness, so is only reasonably accurate under low tension. Although theoretically the stroke of the TSA can be the entire domain of $[0, l_u]$, in reality the thickness of the string prevents a geometric helix from forming once the helix

$$\theta_s = 0 \quad \theta_s = 2\pi \quad \theta_s = 20\pi$$

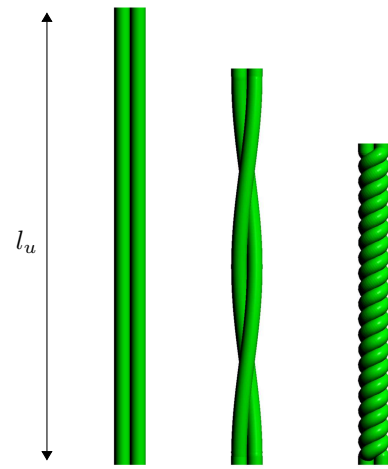


Fig. 1: The value of θ_s increases the number of twists in a string bundle with a string length l_u .

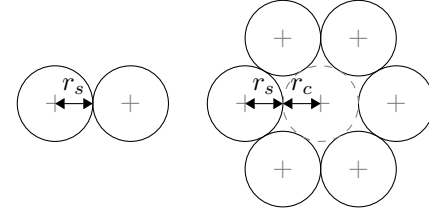


Fig. 2: The location of r_s and optionally r_c in a string bundle.

pitch $q < 4r_s$ (or $q < 2nr_s$ for n strings). This limits the lower bound of the stroke as follows,

$$l_{min} = \frac{l_u}{\sqrt{\frac{\pi^2}{2} + 1}} \approx 0.46 l_u \quad (2)$$

or approximately 46% of l_u for a two string TSA.

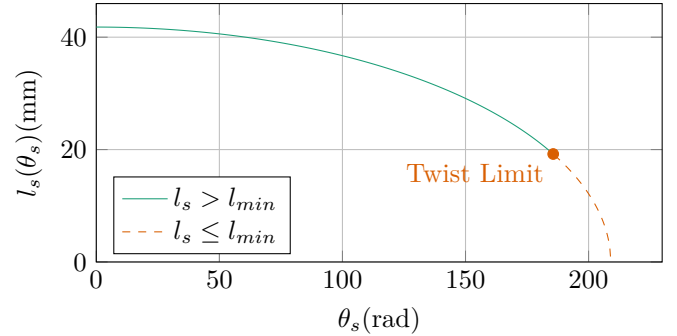


Fig. 3: TSA string length against motor angle with coefficients from table I.

B. Antagonistic Triad

As mentioned in the introduction, because the TSA provides only tensile force, a minimum of three actuators

are required for a 2 DOF actuation system. These can be arranged in a triangular configuration to create an “antagonistic triad”, akin to the antagonistic pairs of muscles found in animals. Where a revolute joint would be found between the connecting ends of the actuator, a universal joint is found instead. By changing the length of each actuator, the angle of the universal joint is altered. The geometric structure of the system as shown in figure 4 can be described with two equilateral triangles of exradius r on two planes separated in the z axis. The centroids are then connected via a universal joint from each plane normal to an intersecting point, let the vector $\boldsymbol{\theta} = [\theta_1 \ \theta_2]$ denote the rotation of the second plane relative to the first, in the x and y axes around the intersecting point, and let l_1 and l_2 denote the normal distance from the intersection to the first and second plane centroids respectively. When $\boldsymbol{\theta} = [0 \ 0]$ the triangles are parallel to each other. The distance between the vertex pairs of each triangle is then denoted as $[\lambda_1 \ \lambda_2 \ \lambda_3]$ for the “top”, “left” and “right” vertices of the triangles. When $\boldsymbol{\theta}$ is changed, this will change λ_1 , λ_2 and λ_3 respectively.

To calculate the lengths of the strings for a given $\boldsymbol{\theta}$ of the universal joint, a transformation matrix for each string

$$\begin{aligned} R_1(\theta_1) &= \begin{bmatrix} \cos \theta_1 & 0 & \sin \theta_1 & 0 \\ 0 & 1 & 0 & 0 \\ -\sin \theta_1 & 0 & \cos \theta_1 & 0 \\ 0 & 0 & 0 & 1 \end{bmatrix} \\ R_2(\theta_2) &= \begin{bmatrix} 0 & 0 & 0 & 1 \\ 0 & \cos \theta_2 & -\sin \theta_2 & 0 \\ 0 & \sin \theta_2 & \cos \theta_2 & 0 \\ 0 & 0 & 0 & 1 \end{bmatrix} \\ P_l(l) &= \begin{bmatrix} 1 & 0 & 0 & 0 \\ 0 & 1 & 0 & 0 \\ 0 & 0 & 1 & l \\ 0 & 0 & 0 & 1 \end{bmatrix} \\ P_r &= \begin{bmatrix} 1 & 0 & 0 & 0 \\ 0 & 1 & 0 & r \\ 0 & 0 & 1 & 0 \\ 0 & 0 & 0 & 1 \end{bmatrix} \\ R_r(\phi) &= \begin{bmatrix} \cos \phi & -\sin \phi & 0 & 0 \\ \sin \phi & \cos \phi & 0 & 0 \\ 0 & 0 & 1 & 0 \\ 0 & 0 & 0 & 1 \end{bmatrix} \end{aligned} \tag{3}$$

$$T_n(\boldsymbol{\theta}) = P_l(l_1) R_1(\theta_1) R_2(\theta_2) P_l(l_2)$$

$$T_1(\boldsymbol{\theta}) = P_r^{-1} T_n(\boldsymbol{\theta}) P_r$$

$$T_2(\boldsymbol{\theta}) = R_r\left(\frac{2\pi}{3}\right) P_r^{-1} R_r\left(-\frac{2\pi}{3}\right) T_n(\boldsymbol{\theta}) R_r\left(\frac{2\pi}{3}\right) P_r$$

$$T_3(\boldsymbol{\theta}) = R_r\left(-\frac{2\pi}{3}\right) P_r^{-1} R_r\left(\frac{2\pi}{3}\right) T_n(\boldsymbol{\theta}) R_r\left(-\frac{2\pi}{3}\right) P_r$$

can be computed, which follows a path from one vertex to the other via the plane normals. This matrix incorporates the universal joint rotations $R_1(\theta_1)$ and $R_2(\theta_2)$, the normal distance translations $P_l(l_1)$ and $P_l(l_2)$, the triangle exradius translation P_r and triangle exradius rotation $R_r(\phi)$, where $\phi = [0, \frac{2\pi}{3}, -\frac{2\pi}{3}]$ to represent the

three vertices of the triangle, hereafter referred to as *top*, *left* and *right*.

Then, to get the distances between the vertex pairs, the euclidean norm for the position components of each transformation matrix \mathbf{T} can be calculated. These distances can then be combined into a vector function $\Lambda(\boldsymbol{\theta}) = [\lambda_1(\boldsymbol{\theta}) \ \lambda_2(\boldsymbol{\theta}) \ \lambda_3(\boldsymbol{\theta})]$ where

$$\begin{aligned} \ell(\mathbf{T}) &= \| [t_{14} \ t_{24} \ t_{34}] \|_2 \\ \Lambda(\boldsymbol{\theta}) &= [\ell(T_1(\boldsymbol{\theta})) \ \ell(T_2(\boldsymbol{\theta})) \ \ell(T_3(\boldsymbol{\theta}))] \\ &= [\lambda_1(\boldsymbol{\theta}) \ \lambda_2(\boldsymbol{\theta}) \ \lambda_3(\boldsymbol{\theta})] \end{aligned}$$

where:

$$\begin{aligned} \lambda_1(\boldsymbol{\theta}) &= \sqrt{l_1^2 + 2l_1l_2 \cos(\theta_1) \cos(\theta_2) + 2l_1r \sin(\theta_2) \cos(\theta_1) + l_2^2 + 2l_2r \sin(\theta_2) - 2r^2 \cos(\theta_2) + 2r^2} \\ \lambda_2(\boldsymbol{\theta}) &= \sqrt{a + b + c - d} \\ \lambda_3(\boldsymbol{\theta}) &= \sqrt{a - b - c + d} \end{aligned}$$

where:

$$\begin{aligned} a &= l_1^2 + 2l_1l_2 \cos(\theta_1) \cos(\theta_2) \\ b &= \sqrt{3}l_1r \sin(\theta_1) - l_1r \sin(\theta_2) \cos(\theta_1) + l_2^2 \\ c &= \sqrt{3}l_2r \sin(\theta_1) \cos(\theta_2) - l_2r \sin(\theta_2) \\ d &= \frac{\sqrt{3}r^2 \sin(\theta_1) \sin(\theta_2)}{2} - \frac{3r^2 \cos(\theta_1)}{2} - \frac{r^2 \cos(\theta_2)}{2} + 2r^2. \end{aligned} \tag{4}$$

The output of this is shown in figure 5 for a domain of $[-\frac{\pi}{2}, \frac{\pi}{2}]$.

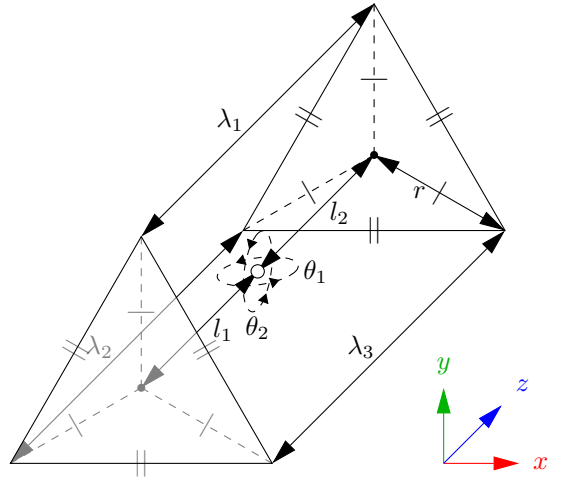


Fig. 4: Kinematic diagram of the antagonistic triad, where the universal joint rotation is defined by $\theta_{1,2}$ on the y and x axes respectively, and the actuator lengths are defined by $\lambda_{1,2,3}$ for the *top*, *left* and *right* strings. r and $l_{1,2}$ define the anchor points of the strings.

II. CONTROL SYSTEM

When initial experiments with a position based control system proved unsuccessful, a force based control system was designed, which uses the dynamics of the AUJ to



Fig. 5: Surface plots of each element of the vector function $\Lambda(\theta)$, assuming coefficient values from table I. For every pair of universal joint angles θ , there is a corresponding vector of actuator lengths $\Lambda(\theta)$. Note that λ_2 and λ_3 are symmetric.

convert angular velocity from a PID controller into angular torque, which is then turned into force setpoints for each TSA using an optimising algorithm. Each TSA has a tensile force when $l_s(\theta_s) < \lambda_n(\theta)$, which is calculated as the difference in triad length and TSA contraction length multiplied by the load stiffness $(\lambda_n(\theta) - l_s(\theta_s)) K_L$. When all of the TSA tensile forces are equal, there is no torque on the AUJ, but when they are unequal, a torque is generated, and if these torques do not match the torques required by the current dynamics to maintain the AUJ orientation, the AUJ will rotate. As the tensile force is measured using load cells, the control system does not need to know the value of K_L since a setpoint force can be maintained using a P controller.

This control system is a four layer cascade design, joining an inverse dynamic control system [11], to the triad force controller in [12], to a proportional controller for each TSA. It uses feedback signals of the joint position from the accelerometers and TSA force from the load cells. A second order setpoint trajectory q is used as the input, which can either be pre-defined or generated dynamically from user input. Feedback is provided by the AUJ angular position θ as shown in figure 4, angular velocity $\dot{\theta}$, and TSA tension force \hat{f} . Figure 7 shows a complete block diagram of the control system.

The control system can be defined by four functions as follows:

- 1) C_1 AUJ Position PID Controller with Acceleration Feedforward
- 2) C_2 Inverse Dynamics
- 3) C_3 TSA Force Optimisation Algorithm
- 4) C_4 TSA Force P Controller

Functions $C_{1\dots 4}$ are then combined into a cascade function $C_4(C_3(C_2(C_1(\dots), \dots), \dots), \dots)$.

A. AUJ Position PID Controller with Acceleration Feed-forward

Firstly, a PID controller is used to generate a control signal u with the input q as the setpoint, and the AUJ angular position θ and velocity $\dot{\theta}$ as feedback, plus the addition of a feedforward term for the input acceleration \ddot{q} .

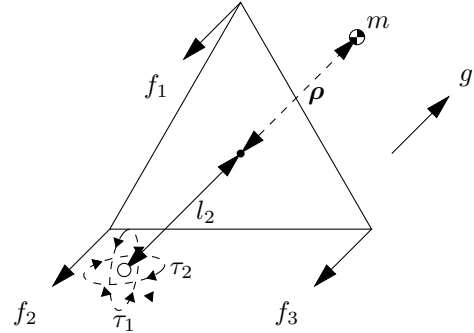


Fig. 6: Dynamics of an antagonistic triad based on figure 4, where the follower mass is m , the follower center of mass (COM) relative to the universal joint pivot is ρ , the forces on each anchor point are $f_{1,2,3}$ and the universal joint torque is $\tau_{1,2}$.

In the discrete implementation used for fixed step simulation and experimental system control, the integral term is replaced by the trapezoidal rule.

B. Inverse Dynamics

The control signal u from the PID controller is then converted to the desired AUJ torque τ . This is achieved using the Euler-Lagrange formulation which takes into account the dynamic properties of the AUJ in its current state, as shown in figure 6. For simplicity, the mass of the universal joint is ignored and the value of ρ only has a z component, ρ_3 , which is included in the experiments in section IV-C4 but set to zero for all other experiments. The torque is calculated as $\tau = D(\theta) u + C(\theta, \dot{\theta}) \dot{\theta} + G(\theta)$ with the functions from (5).

C. TSA Force Optimisation Algorithm

This uses the *inverse force transformation* algorithm from [12] with the jacobian of equation 4 to select an optimal force vector from the desired joint torque. Here it is presented in an unexpanded and more general form,



Fig. 7: Block diagram of the complete experimental control system, excluding the hardware velocity controllers for the motors.

$$\begin{aligned}
 T^\tau(\boldsymbol{\theta}) &= R_1(\theta_1) R_2(\theta_2) P_l(l_2 + \rho_3) \\
 J_v(\boldsymbol{\theta}) &= J([t_{14}^\tau \quad t_{24}^\tau \quad t_{34}^\tau]) = \begin{bmatrix} (l_2 + \rho_3) \cos \theta_1 \cos \theta_2 & (-l_2 - \rho_3) \sin \theta_1 \sin \theta_2 \\ 0 & (-l_2 - \rho_3) \cos \theta_2 \\ (-l_2 - \rho_3) \sin \theta_1 \cos \theta_2 & (-l_2 - \rho_3) \sin \theta_2 \cos \theta_1 \end{bmatrix} \\
 J_\omega(\boldsymbol{\theta}) &= J \left(\dot{\theta}_1 \begin{bmatrix} 0 \\ 1 \\ 0 \end{bmatrix} + \dot{\theta}_2 R_2(\theta_2)^r \begin{bmatrix} 1 \\ 0 \\ 0 \end{bmatrix} \right) = \begin{bmatrix} 0 & \cos \theta_1 \\ 1 & 0 \\ 0 & -\sin \theta_1 \end{bmatrix} \\
 D(\boldsymbol{\theta}) &= m J_v^\top J_v + J_\omega^\top R_1(\theta_1)^r R_2(\theta_2)^r I (R_1(\theta_1)^r R_2(\theta_2)^r)^\top J_\omega \\
 &= \text{diag} \left(\begin{bmatrix} I_{22} \cos^2 \theta_2 - I_{33} \cos^2 \theta_2 + I_{33} + l_2^2 m \cos^2 \theta_2 + 2l_2 m \rho_3 \cos^2 \theta_2 + m \rho_3^2 \cos^2 \theta_2 \\ I_{11} + l_2^2 m + 2l_2 m \rho_3 + m \rho_3^2 \end{bmatrix}^\top \right) \quad (5) \\
 C(\boldsymbol{\theta}, \dot{\boldsymbol{\theta}}) &= C^{k \times j} \mid c_{k,j} = \sum_{i=1}^N \frac{1}{2} \left(\frac{\partial d_{kj}}{\partial \theta_i} + \frac{\partial d_{ki}}{\partial \theta_j} - \frac{\partial d_{ij}}{\partial \theta_k} \right) \dot{\theta}_i \\
 &= \begin{bmatrix} \frac{(-I_{22} + I_{33} - l_2^2 m - 2l_2 m \rho_3 - m \rho_3^2) \sin(2\theta_2) \dot{\theta}_2^2}{2} & \frac{(-I_{22} + I_{33} - l_2^2 m - 2l_2 m \rho_3 - m \rho_3^2) \sin(2\theta_2) \dot{\theta}_1^2}{2} \\ \frac{(I_{22} - I_{33} + l_2^2 m + 2l_2 m \rho_3 + m \rho_3^2) \sin(2\theta_2) \dot{\theta}_1^2}{2} & 0 \end{bmatrix} \\
 P(\boldsymbol{\theta}) &= mg T^\tau \\
 G(\boldsymbol{\theta}) &= J(p_{34}) = [-gm(l_2 + \rho_3) \sin \theta_1 \cos \theta_2 \quad -gm(l_2 + \rho_3) \sin \theta_2 \cos \theta_1]
 \end{aligned}$$

$$\begin{aligned}
 J_\Lambda &= \begin{bmatrix} \frac{\partial \lambda_1}{\partial \theta_1} & \frac{\partial \lambda_2}{\partial \theta_1} & \frac{\partial \lambda_3}{\partial \theta_1} \\ \frac{\partial \lambda_1}{\partial \theta_2} & \frac{\partial \lambda_2}{\partial \theta_2} & \frac{\partial \lambda_3}{\partial \theta_2} \end{bmatrix} \\
 \gamma(i) &= -J_{\Lambda_{-i,*}}^{-\top} \left(J_{\Lambda_{i,*}}^\top f_{\min} + \boldsymbol{\tau} \right) \quad (6) \\
 \mathbf{F}(\boldsymbol{\tau}, \boldsymbol{\theta}) &= \begin{bmatrix} f_{\min} & \gamma(2)_1 & \gamma(3)_1 \\ \gamma(1)_1 & f_{\min} & \gamma(3)_2 \\ \gamma(1)_2 & \gamma(2)_2 & f_{\min} \end{bmatrix}.
 \end{aligned}$$

A force matrix \mathbf{F} is created from the torque input $\boldsymbol{\tau}$, jacobian J_Λ from the vector function Λ as defined in equation 4, and minimum force constant f_{\min} . f_{ii} is equal to f_{\min} , while the other elements in the column are based on a calculation using $J_{\Lambda_{-i,*}}$ where $-i$ is a row removed from the matrix.

The following algorithm then selects one column of \mathbf{F} to be the output force vector \mathbf{f} , where \top and \perp are boolean *true* and *false* respectively, and $\mathbf{f}_{*,i}$ is the i th column of \mathbf{F} . The solution to this algorithm minimises the net force

on all TSA while producing the desired output torque on the universal joint.

```

1:  $s \leftarrow [\top \quad \top \quad \top]$ 
2: if  $f_{23} > f_{\min}$  then  $s_2 \leftarrow \perp$  else  $s_3 \leftarrow \perp$  end if
3: if  $f_{31} > f_{\min}$  then  $s_3 \leftarrow \perp$  else  $s_1 \leftarrow \perp$  end if
4: if  $f_{12} \geq f_{\min}$  then  $s_1 \leftarrow \perp$  else  $s_2 \leftarrow \perp$  end if
5: for  $i = 1$  to  $3$  do
6:   if  $s_i \rightarrow \top$  then  $\mathbf{f} \leftarrow \mathbf{f}_{*,i}$  end if
7: end for

```

D. TSA Force Proportional Controller

The selected forces are then used as an input to a P controller with gain k_{ps} using the measured load cell forces $\hat{\mathbf{f}}$ as feedback. The output from this can then be used to control the top, left and right TSA motors, corresponding to the actuators in figure 4. A deadband controller was used to compensate for motor limitations, which is further discussed in section IV-B1.

III. SIMULATION DESIGN

To design and refine the parameters of the control system, a Simscape Multibody™ model of the antagonistic triad and control system was created in MATLAB®/Simulink™. This allowed for model design coefficients $l_{1,2}$ and controller gains k_p, k_i, k_d, k_{ps} to be modified in order to have the most stable control within design limits, as shown in table II.

In the simulation, each TSA was modelled as a state-space system

$$\begin{aligned} h(\theta_s) &= \frac{\theta r_s^2}{\sqrt{l_u^2 - \theta_s^2 r_s^2}} \\ k(\theta_s, \theta) &= \lambda_n(\theta) - \sqrt{l_u^2 - \theta_s^2 r_s^2} \\ \dot{x} &= \begin{bmatrix} x_2 \\ -\frac{K_L}{J} h(x_1) k(x_1, \theta) - \frac{C}{J} \operatorname{sgn}(x_2) \end{bmatrix} + \begin{bmatrix} 0 \\ \frac{K_t}{J} \end{bmatrix} u \\ y &= K_L \operatorname{sat}_0^\infty k(x_1, \theta), \end{aligned} \quad (7)$$

modified from [4], which takes motor current u as an input and outputs y as the TSA tension force, where J is the motor inertia, C is the motor coulomb friction (modified from viscous friction as the motor only has dry friction), K_t is the motor torque constant, and K_L is the load stiffness. As the original definition is for a fixed load l_u distance from the motor a modified model is required which takes into account the varying length between the motor and load defined by $\Lambda(\theta)$.

A saturation function, with the compact notation $\operatorname{sat}_x^y z = \max(x, \min(y, z))$ is used to prevent incorrect compression forces when the string is slack. All of the motor coefficients were taken from the Faulhaber 1724TSR datasheet [13] as this is the motor used in the experimental model. An estimated value is used for the load stiffness, this was chosen to be a high number as the model is expected to be very stiff.

The state space model was then adapted to include constraints on motor velocity and acceleration set by the motor controller in order to keep the motor within design limits,

$$\dot{x}' = \begin{bmatrix} \operatorname{sat}_{-\omega_s}^{\omega_s} \dot{x}_1 \\ \operatorname{sat}_{-\alpha_s}^{\alpha_s} \dot{x}_2 \end{bmatrix}, \quad (8)$$

which replaces \dot{x} with \dot{x}' , which contain saturation functions for maximum motor velocity v_s and acceleration α_s .

Based on a combination of simulation modelling, motor parameters, and physical design constraints, the model parameters were set to the values in table I. l_2 was set to zero, as this produced the most stable control system in simulation.

TABLE II: PID gains in the simulation and experiment.

Gain	Value	
	Simulation	Experiment*
k_p	800	3×10^4
k_i	3000	350
k_d	50	50
k_{ps}	19	100

* Tracking mode, see section IV-B2.

IV. EXPERIMENTS

TABLE I: Model coefficients.

Coefficient	Value	Coefficient	Value
l_1	41.8 mm	J	$1 \times 10^{-6} \text{ kg m}^{-2}$
l_2	0 mm	K_L	1000 N m^{-1}
r	13 mm	f_{min}	3 N
l_u	41.8 mm	ω_s	441.9 rad s^{-1}
r_s	200 μm	I_s	0.19 A
m	72.619 13 g	K_t	$0.0263 \text{ N m A}^{-1}$
C	0.1315 N mm	τ_s	4.5 mN m
α_s	$1 \times 10^5 \text{ rad s}^{-2}$	ρ	$[0 \ 0 \ 0] \text{ mm}$
Coefficient	Value		
I	$\begin{bmatrix} 3 \times 10^{-5} & 0 & 0 \\ 0 & 3.2 \times 10^{-5} & 0 \\ 0 & 0 & 1.4 \times 10^{-5} \end{bmatrix} \text{ kg m}^{-2}$		

For the experimental validation, a physical prototype of the mechanism was constructed with coefficients from table I as design parameters. This was mounted vertically, in order for the inertial measurement unit (IMU) to measure the orientation of the universal joint. The TSA mechanisms consist of a compact high torque motor attached to the base segment, with a string clamp attached to the motor shaft. On the follower segment, a load cell is mounted on top of a universal joint to ensure a purely axial load, with a capstan bolt attached to the load cell. The string itself is attached to the clamp at both ends using two grub screws for extra security and easy adjustment, and looped through the hole in the capstan bolt. The total mass of the prototype, excluding the mount, is $\approx 176 \text{ g}$. Figures 8 and 9 detail the construction of the experiment with all the constituent parts.

The motors were controlled by Fauhaber MCDC3002 motor controllers, which could interface with a National Instruments MyRIO via the USB port, using a USB to serial converter. The load cells were Futek LCM100 miniature load cells, selected for their small size. The signals from these were amplified using Flyde FE-359-TA instrumentation amplifiers and decoded using an external AD7606 ADC before being fed into the MyRIO using SPI. The orientation of the AUJ was measured using a Bosch Sensortec BNO080 IMU using the accelerometer data. Due to the poor resolution of the IMU data, which is discussed in section V-D, the pitch and roll data in figures 15 to 19 have a Savitsky-Golay filter applied with a window length of 11 and an order of 1.

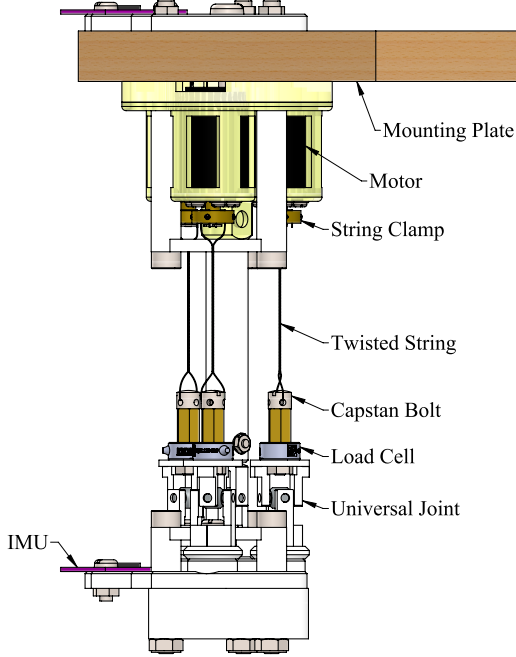


Fig. 8: Schematic of the experimental system with labelled components.

A. Force Proportional Controller & Motor Characterisation

Before verifying robust control of the AUJ, the control of each individual TSA needed to be tested in order to characterise the performance of the motors and to ensure the inner loop control system was robust. This would involve selecting the control strategy that gave the best performance. A test trajectory consisting of a smooth ramp followed by a sine wave was fed into the inner loop of the cascade function as $[f(t) \ f(t) \ f(t)]$. Each control strategy was tested, and in the end the velocity control strategy proved most optimal, as is shown in figure 13. The results of a sinusoidal force trajectory for the velocity control strategy is shown in figure 14. As can be seen in the inset, there is a stick-slip friction effect which causes a sawtooth like effect on the measured force. This means the motor angle has to be constantly adjusted even with a constant force input, in order to maintain the setpoint force.

1) *Direct current control (DCC)*: This mode takes a preset velocity $\dot{\theta}_{set} \in [0, 4220]$ and uses a hardware PI controller with velocity feedback $\dot{\theta}_{act}$ to generate a control voltage. This voltage \mathbf{V} is then multiplied by the signum of the result from the cascade function in order to ensure the motor spins in the right direction, and then passed to a current limiter with the current error (the result with the actual current I_{act} subtracted) as the limit, before being sent to the motor. This ensures the motor stops spinning when the target current is reached. \mathbf{V} is calculated as

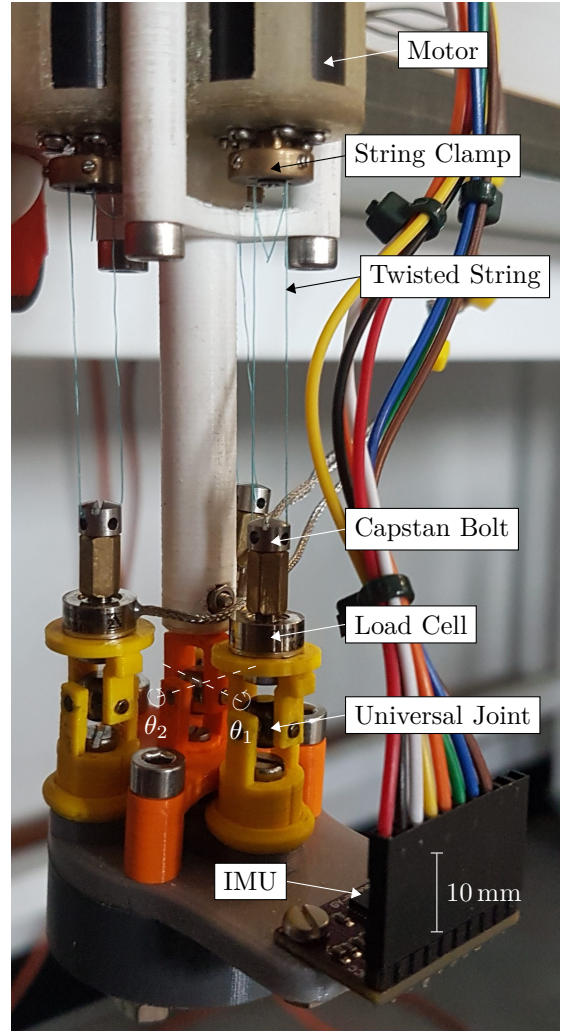


Fig. 9: Annotated photograph of the experimental model, with the roll θ_1 and pitch θ_2 axes marked.

$$\epsilon_c = \dot{\theta}_{set} - \dot{\theta}_{act}$$

$$\mathbf{V} = \left(K_{P_c} \epsilon_c + K_{D_c} \int_0^t \epsilon_c \right) \text{sgn}(C_4(\dots)) \omega(C_4(\dots) - I_{act}), \quad (9)$$

where $\omega(\dots) \in [0, 1]$ is an unknown hardware limiting function that controls the motor speed depending on the current error.

2) *Proportional Current Controller*: This strategy is a more direct method of current control, using a software P controller to directly set the voltage of the motor, using the MCDC 3002 as simply a passive amplifier. In this case the current error is passed directly to a P controller which has its output limited to prevent damage to the motors. \mathbf{V} is calculated as

$$\mathbf{V} = K_{P_c} C_4(\dots) - I_{act}. \quad (10)$$

3) *Velocity Control*: This strategy simply uses the result from the cascade function as a velocity setpoint using the hardware velocity PI controller. \mathbf{V} is calculated as

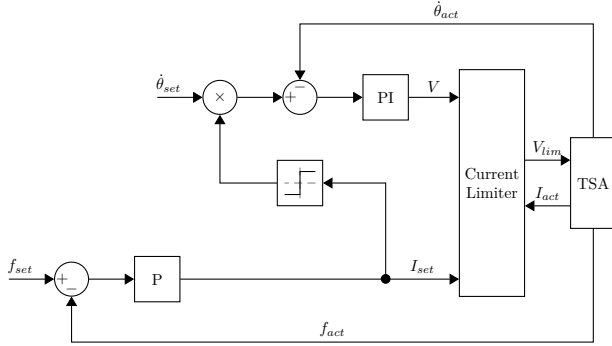


Fig. 10: Block diagram of the DCC.

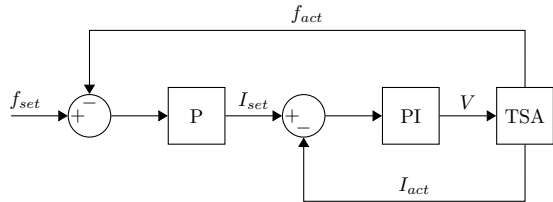


Fig. 11: Block diagram of the proportional current controller.

$$\mathbf{V} = K_{P_c} \boldsymbol{\epsilon}_c + K_{D_c} \int_0^t \boldsymbol{\epsilon}_c. \quad (11)$$

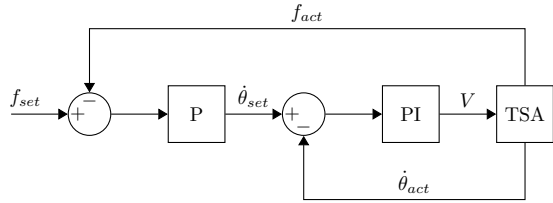


Fig. 12: Block diagram of the velocity controller.

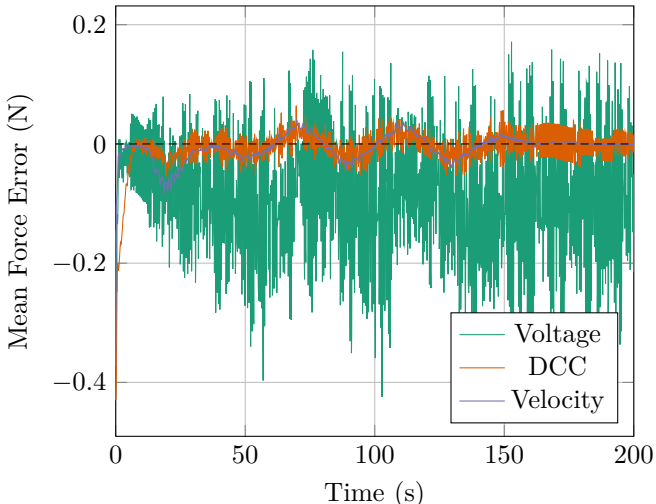


Fig. 13: Mean tracking error for each control strategy.

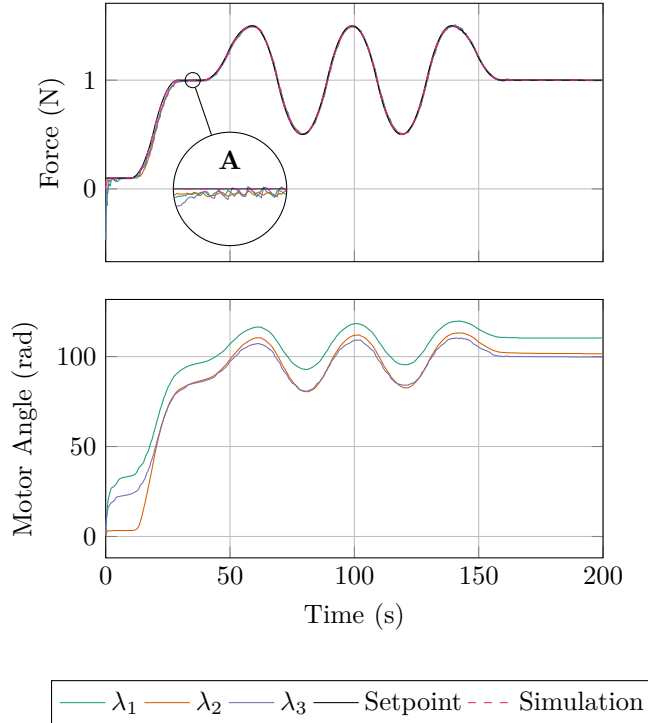


Fig. 14: Load cell, motor angle, and motor velocity signal plot from each string using the velocity control strategy for an experimental trajectory. Inset A shows a zoomed in portion of the graph, illustrating the stick-slip phenomenon noticed in the load cell measurements.

B. Modifications to Control System

1) *Experimental Velocity Control with Deadband Compensation:* Due to a controller deadband within $\pm 10 \text{ min}^{-1}$, an adjustable deadband compensator is used,

$$\phi_i(\omega_i) = \begin{cases} 10 & 10 \leq \omega_i < h \\ -10 & -h < \omega_i \leq -10 \\ 0 & h \leq \omega_i \leq -h \\ \omega_i & \text{otherwise} \end{cases} \quad (12)$$

where ϕ_i is the compensator for the controller i . An adjustment value $h \in [0, 10]$ changes the threshold at which the compensator switches on and off, allowing for a small deadband to remain.

2) *Windup & Tracking States:* When the mechanism is started with the TSA in a completely unwound state, before it can begin tracking a motion trajectory, the TSA strings must “wind up” to closely match the initial state of \mathbf{f} . During this phase, the outer PID gains $\mathbf{k}_p, \mathbf{k}_i$ are unsuitable and can result in damage to the mechanism. To mitigate this, two sets of PID gains are chosen, one for the windup state ($\mathbf{k}_p = 800, k_i = 3000$), and another for the tracking state ($\mathbf{k}_p = 3 \times 10^4, k_i = 350$), which the windup state transitions to once suitable stability is achieved. This transition trigger is defined on a per-axis basis, as the first zero crossing of the angle error (as $\mathbf{q} = 0$ this is effectively θ). A graph showing the difference this

state change makes to the AUJ orientation is shown in figure 15.

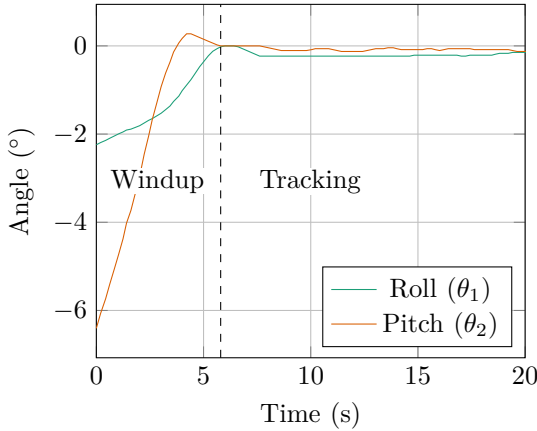


Fig. 15: The initial startup of the mechanism showing the transition between “windup” and “tracking” states.

C. AUJ Experiments

1) *AUJ Angle Tracking*: Figure 16 plots the tracking response of both the simulation and experiment. Three trajectories were created to test the capabilities of the mechanism. Two were only in one axis of the Universal Joint, and the third was in both axes.

2) *The Effect of f_{\min} on AUJ Roll Range Limits*: Ultimately the AUJ range limits are determined by the angle at which one or more of the TSA are “fully unwound” where $l_s(\theta_s) = l_u$, or “fully wound” where $l_s(\theta_s) = l_{\min}$, unless there is a string failure before this limit. If f_{\min} is increased, the length of each TSA at $\theta = [0, 0]$ is reduced, as a greater difference between $\lambda_n(\theta)$ and $l_s(\theta_s)$ is needed for a larger tensile force, as described in section II. Therefore, increasing f_{\min} should increase the AUJ angle range as there is a greater difference between the length of the TSA at $\theta = [0, 0]$ and a fully unwound TSA, as long as there is sufficient length available so an antagonist TSA doesn’t become fully wound.

An experiment was set up where the setpoint angle of the AUJ would continually linearly increase, after a short period of acceleration, on the roll (θ_1) axis. The control system monitored the motor angles of each TSA, and halted the experiment when any TSA motor angle was at or below 2π , as a safety margin to prevent damage to the mechanism. The AUJ angle at the end of the experiment was recorded, as shown in figure 17. By repeating the experiment with increasing values of f_{\min} , it was possible to determine how it affected the maximum roll angle. These experiments were able to achieve modest increases of $\approx 4.004^\circ \text{N}^{-1}$ for the positive (upper) limit of the universal joint roll θ_1 , and $\approx -6.062^\circ \text{N}^{-1}$ for the negative (lower) limit, within the f_{\min} interval [3, 3.5]. Attempts to increase the upper bound of this interval resulted in string failure, possibly due to $l_s(\theta_s)$ exceeding l_{\min} but it was not possible to conclusively determine this. Similar

TABLE III: Trapezoidal trajectory sequence parameters.

Cycle	Max./Min. Angle [rad]	Max. Velocity [rad s ⁻¹]	Acceleration [rad s ⁻²]
1	0.2	0.01	0.00125
2	0.2	0.03	0.02125
3	0.2	0.05	0.04125
4	0.2	0.07	0.06125

experiments for the pitch angle resulted in string failure before any TSA fully unwound even at $f_{\min} = 3$.

A better solution for increasing AUJ range limits is to reduce the value of r , as is discussed in section V-C.

3) *The Effect of AUJ Angular Velocity on AUJ Angle Tracking*: To verify the performance of the AUJ at higher angular velocities, the single axis experiments from section IV-C1 were repeated with a trapezoidal “chirp” signal, with the maximum angular velocity increasing by $\omega_0 + (2(n-1)\omega_0)$ each cycle, where n is the cycle number, and ω_0 is the initial maximum angular velocity, and the angular acceleration increasing by $\alpha_0 + (16(n-1)\alpha_0)$ each cycle, where α_0 is the initial angular acceleration. A total of four cycles were performed, with the maximum velocity and acceleration values shown in table III. Figure 18 shows the results of these experiments, which shows the tracking error increasing marginally as maximum angular velocity and acceleration increases.

4) *The Effect of Follower Mass on AUJ Angle Tracking*: In order to demonstrate the feasibility of a multiple joint system, additional mass was added to the follower segment and the *Pitch & Roll* trajectory was performed to analyze the effect of the additional mass on the control system. This was performed by the modification of the end of the follower segment to allow multiple standard disc weights, each with a mass of 100g, to be attached. Four experiments were performed, one with no disc weights attached, and three with one, two, and three disc weights attached, adding approximately 100g each time. 3D printed custom length spacers were used to maintain an approximately equal COM for each of the experiments with disc weights. Table IV lists the four follower mass configurations that were tested, with follower mass and inertia matrix m and I , and follower COM z component ρ_3 , along with a figure for each configuration. The follower COM x and y components were set to 0 for these experiments, as they did not vary significantly between experiments, and had a negligible contribution to the dynamics. These figures are based on estimates from a computer aided design (CAD) model developed in SolidWorks®, with known weights of 100g. Any inertial terms less than 1×10^{-5} were rounded down to 0, which resulted in a diagonal inertia matrix. For each experiment, the inverse dynamics parameters m and ρ were updated so the correct setpoint torque would be calculated.

Figure 19 shows the setpoint and response trajectory for each experiment. Initially, k_p was set to the same value as in table I, however the system was unable to reach a steady state in any configuration other than “No Mass”.



Fig. 16: Plots of the response for three different trajectories, one on only the roll axis θ_1 (column 1), one on only the pitch axis θ_2 (column 2), and one on both axes θ_1 and θ_2 (column 3). Plots include AUJ orientation, forces at the top, left and right TSA, and the motor positions. Note the simulation error is very small, so the plot cannot be seen on the graph.

TABLE IV: Table of all the follower mass configurations, with the parameters for follower mass m and follower COM z offset ρ_3 .

Configuration	m [g]	ρ_3 [mm]	I [kg m $^{-2}$]	Image
No Mass	67	6.7	$\begin{bmatrix} 3.3 \times 10^{-5} & 0 & 0 \\ 0 & 3.1 \times 10^{-5} & 0 \\ 0 & 0 & 1.4 \times 10^{-5} \end{bmatrix}$	
+100 g	170	49	$\begin{bmatrix} 1.3 \times 10^{-4} & 0 & 0 \\ 0 & 1.3 \times 10^{-4} & 0 \\ 0 & 0 & 4.6 \times 10^{-5} \end{bmatrix}$	
+200 g	220	50	$\begin{bmatrix} 1.7 \times 10^{-4} & 0 & 0 \\ 0 & 1.7 \times 10^{-4} & 0 \\ 0 & 0 & 7.7 \times 10^{-5} \end{bmatrix}$	
+300 g	320	50	$\begin{bmatrix} 2.0 \times 10^{-4} & 0 & 0 \\ 0 & 2.0 \times 10^{-4} & 0 \\ 0 & 0 & 1.1 \times 10^{-4} \end{bmatrix}$	

Reducing k_p to 1000 in the weighted configurations solved the steady state issue and resulted in an average maximum tracking error of 0° over all configurations with added mass, similar to the result from the initial experiments. However, for the “No Mass” configuration, $k_p = 1000$ resulted in a very poor tracking response, whereas k_p from table I resulted in a maximum tracking error of 0° , once again similar to the result from the initial experiments. In future implementations gain scheduling can be employed to select the most optimal k_p for a given follower mass, that allows for the smallest tracking error while being able to reach a steady state.

V. DISCUSSION

A. TSA Comparison with Leadscrew and Direct Drive

To compare the performance of a TSA AUJ against alternatives, we can measure two metrics, the maximum tension force f_{max} and maximum stroke velocity \dot{p}_{max} . This corresponds to the equivalent of maximum torque and maximum velocity in a rotary motor, a larger f_{max} would be able to actuate a larger follower mass, and a larger \dot{p}_{max} would be able to rotate the AUJ more quickly. The alternatives chosen for comparison are leadscrews of various rod diameters d_m and pitches λ , and a “direct drive” where the motor is rotating the universal joint directly without any reduction or motion transformation, as shown in figure 20.

1) *Twisted string actuator:* For the TSA metrics, the equations from [4], in particular $h(\theta)$ and $k(\theta)$ as used for the state space, which can be used to determine f_{max} and \dot{p}_{max} . By extracting coefficient r_s as an input to make

$f(p, r_s)$ and $\dot{p}(\dot{\theta}, p, r_s)$ the performance of different string thicknesses can be compared for a given unwound length l_u and $\tau_{max}, \dot{\theta}_{max}$ over the range of the contraction length p . f_{max} is calculated as

$$\begin{aligned} k(\theta) &= l_u - \sqrt{l_u^2 - \theta_s^2 r_s^2} \\ k^{-1}(p) &= \pm \frac{\sqrt{p(2l_u - p)}}{r_s} \\ h^{-1}(\theta) &= \frac{\sqrt{l_n^2 - r_s^2 \theta^2}}{r_s^2 \theta} \\ f(p) &= h^{-1}(k^{-1}(p)) = \pm \frac{\sqrt{(l_u - p)^2}}{r_s \sqrt{p(2l_u - p)}} \\ f_{max} &= f(p)\tau_{max}, \end{aligned} \quad (13)$$

and \dot{p}_{max} is calculated as

$$\begin{aligned} \dot{k}(\dot{\theta}, \theta) &= \frac{\dot{\theta} r_s^2 \theta}{\sqrt{l_u^2 - r_s^2 \theta^2}} \\ \dot{p}(\dot{\theta}, p) &= \dot{k}(\dot{\theta}, k^{-1}(p)) = \pm \frac{\dot{\theta} r_s \sqrt{p(2l_u - p)}}{\sqrt{(l_u - p)^2}} \\ \dot{p}_{max} &= \dot{p}(\dot{\theta}_{max}, p). \end{aligned} \quad (14)$$

2) *Leadscrew:* For the leadscrew metrics, the raising torque calculation [14] can be used as the absolute value of f_{max} , since the TSA only operates in tension, which can be used to determine the same metrics. The performance of different screw diameters d_m and leads λ can then be compared for a given τ_{max} and coefficient of friction μ .

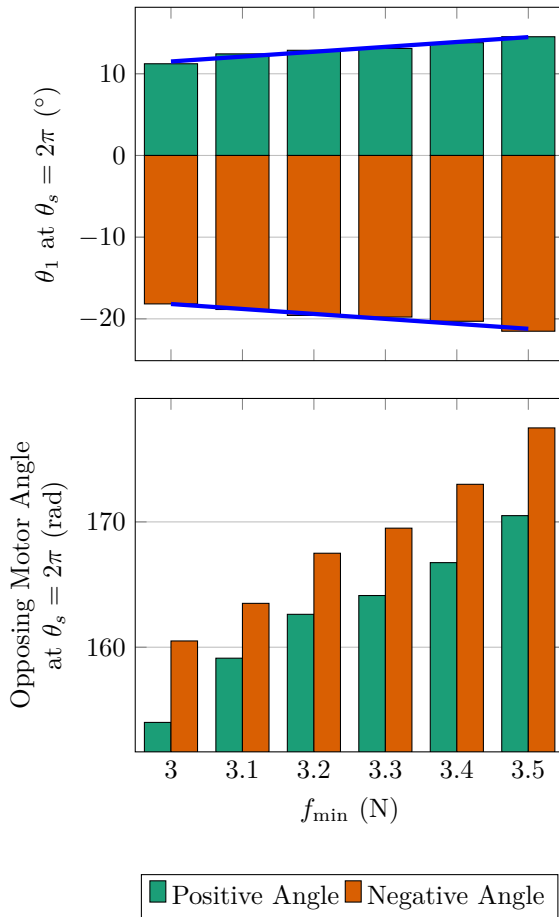


Fig. 17: AUJ roll angle (θ_1) when the smallest TSA motor angle is equal to 2π , and motor angle of the “opposing” TSA (the TSA with the largest motor angle) at the same position.

\dot{p}_{max} is then calculated by multiplying λ with $\dot{\theta}_{max}$. The performance of different λ can then be compared for a given $\dot{\theta}_{max}$. f_{max} is calculated as

$$\begin{aligned} |\tau(f)| &= \frac{d_m f (\lambda + \pi d_m \mu)}{2(\pi d_m - \lambda \mu)} \\ |f(\tau)| &= \frac{2\tau(\pi d_m - \lambda \mu)}{d_m (\lambda + \pi d_m \mu)} \\ f_{max} &= |f(\tau_{max})|, \end{aligned} \quad (15)$$

and \dot{p}_{max} is calculated as

$$\begin{aligned} \dot{p}(\dot{\theta}) &= \lambda \frac{\dot{\theta}}{2\pi} \\ \dot{p}_{max} &= \dot{p}(\dot{\theta}_{max}). \end{aligned} \quad (16)$$

3) *Direct Drive*: The direct drive metrics are trivially calculated using the lever force and tangential velocity that would be generated at the endpoint of a linear actuator able to impart equivalent angular velocity and torque on the universal joint. f_{max} is calculated as

$$f_{max} = \frac{\tau_{max}}{\sqrt{l_2^2 + r^2}}, \quad (17)$$

and \dot{p}_{max} is calculated as

$$\dot{p}_{max} = \dot{\theta}_{max} \sqrt{l_2^2 + r^2}. \quad (18)$$

4) *Comparison between TSA and Leadscrew*: As the values for τ_{max} and $\dot{\theta}_{max}$ for the TSA depend on p , but remain constant for the leadscrew, the performance of the TSA is going to be better or worse than a given leadscrew depending on the value p . Figure 21 compares the TSA configuration using the coefficients from table I against a number of common leadscrew configurations that are practical for the dimensions of the AUJ. The TSA outperforms or underperforms different leadscrew configurations depending on p . In simpler terms, the performance of the TSA is dependent on the contraction length. The maximum linear velocity increases with the contraction length, and the maximum tension force decreases with contraction length, both in a nonlinear fashion.

B. Monofilament Torsion Fatigue & String Breakage

TSA string breakage was common during experiments, this was often due to a loss of control stability during tuning, or operation beyond previously explored motor angle or load limits. However, failure rates were observed to increase with the number of working cycles (winding and unwinding) of each TSA string, particularly when taken to high motor angles or loads. Nylon monofilament, as was used for the TSA string, is susceptible to torsion fatigue [15], [16] which reduces tensile strength [17]. This decrease in strength could be a potential explanation for the increase in failure rate. There was also the route and securing method of the string itself, which used four grub screws to clamp onto the string to hold both ends in place, and also passed close to six potentially sharp edges, as shown in figure 22. These locations could weaken the string, by either an edge biting into it when under high tension, or when being clamped by the grub screws.

The cause of the string break could be determined by the location of the break. If it was located at or near one of the grub screws or biting edges, then it was likely to be caused by those. If it was located on the “active” part of the string that twists, then torsion fatigue is likely to be the culprit. To somewhat mitigate the biting and clamping issue, polytetrafluoroethylene (PTFE) sleeving was added around the string near those locations, and this did result in a significant reduction in string breakages due to edge biting or clamping. This could be improved upon by redesigning the string clamp and capstan to round off sharp edges, and to consider alternatives to clamping such as end knotting or loop wrapping.

The experiments in [18] used 0.2 mm Dyneema® and Fast Flight® Plus polyethylene (PE) polyfilament, and were able to achieve over 1000 working cycles before failure at a load of ≤ 20 N at a motor angle of nearly 300 rad. Use of nylon monofilament was purely for convenience, assembly of polyfilament was difficult as slicing the ends usually resulted in individual fibres splaying, which made it impossible thread through the string clamp. A redesign

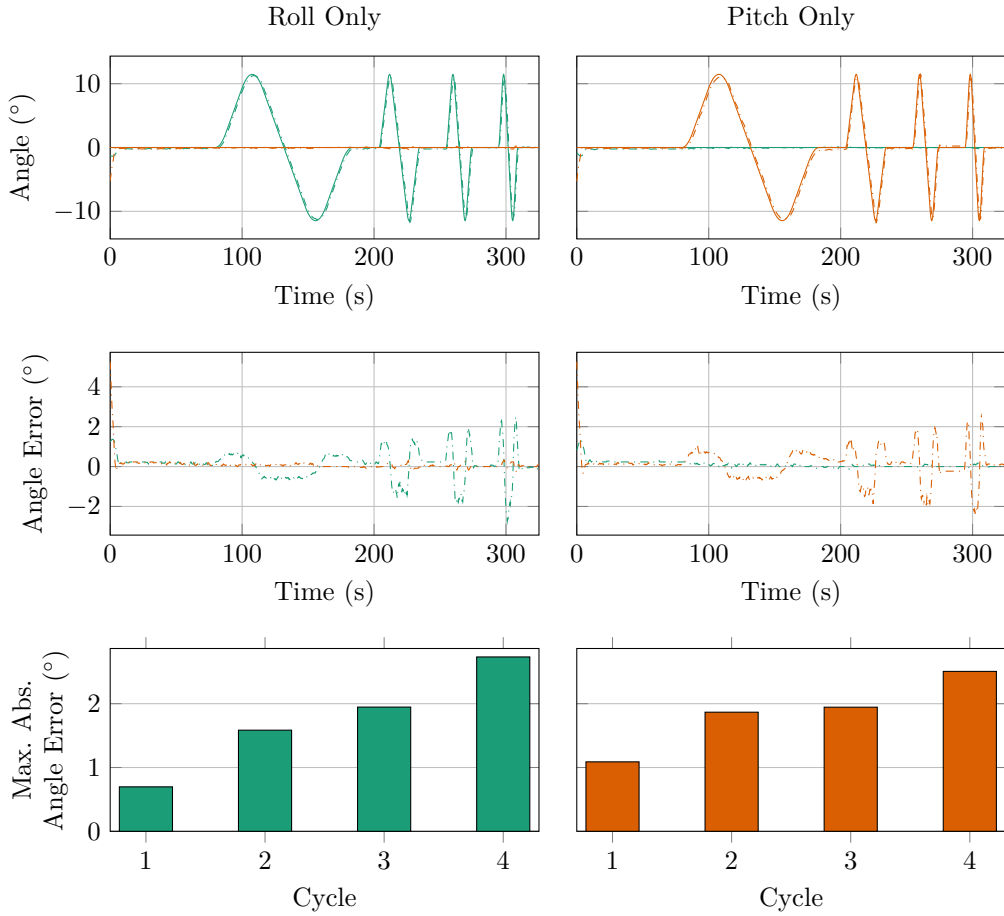


Fig. 18: Results of the trapezoidal velocity trajectory from table III for both AUJ pitch and roll trajectories, including the maximum absolute angle error for each cycle.

of the string clamp could make it easier to use polyfilament, which based on the results from [18] could greatly improve string longevity.

C. Improving AUJ Angle Range & Enabling Active Transmission Adjustment by Reducing Triad Radius

As can be seen in figure 23, decreasing the triad radius r decreases the stroke range of each TSA for a given AUJ angle range. This increases the AUJ angle range limits without having to increase f_{min} as was done in section IV-C2.

If r or the AUJ angle range is small enough, this allows for active transmission adjustment, where increasing or decreasing f_{min} shifts the active TSA stroke “window” to the right or left along the maximum force and maximum velocity curves from figure 21, as shown in figure 24. This would allow the performance of the AUJ to be adjusted during operation, which could be useful in some applications, such as a mobile snake robot which could increase AUJ angular velocity when all segments are on the ground, and sacrifice angular velocity in some segments for increased AUJ torque when they are off the ground and therefore subject to gravitational forces.

An issue with a small triad radius is the difficulty of accommodating the central shaft with the universal joint. This can be solved by using a wide universal joint with a hollow spider, which allows the three TSA to pass through the middle of the joint and the central shaft is not required, as shown in figure 25.

D. Hardware Improvements

Using the BNO080 as the AUJ orientation sensor proved to be challenging. The magnetometer was unusable within the indoor experimental environment even after several calibration attempts, so the universal joint angle would not be able to be calculated when the gravity vector is not orthogonal to the universal joint DOF, hence the experiments had the AUJ in a vertical orientation. The accelerometer data from the IMU, used to calculate the AUJ orientation, was of poor resolution as can be seen in figure 26.

An alternative method for sensing the AUJ orientation could be used, such as linear variable differential transformers (LVDTs), hall effect sensors or potentiometers. If the hollow spider universal joint design in section V-C is used, the larger spider pins would be able to accommodate potentiometers. The 1724TSR motors also had poor

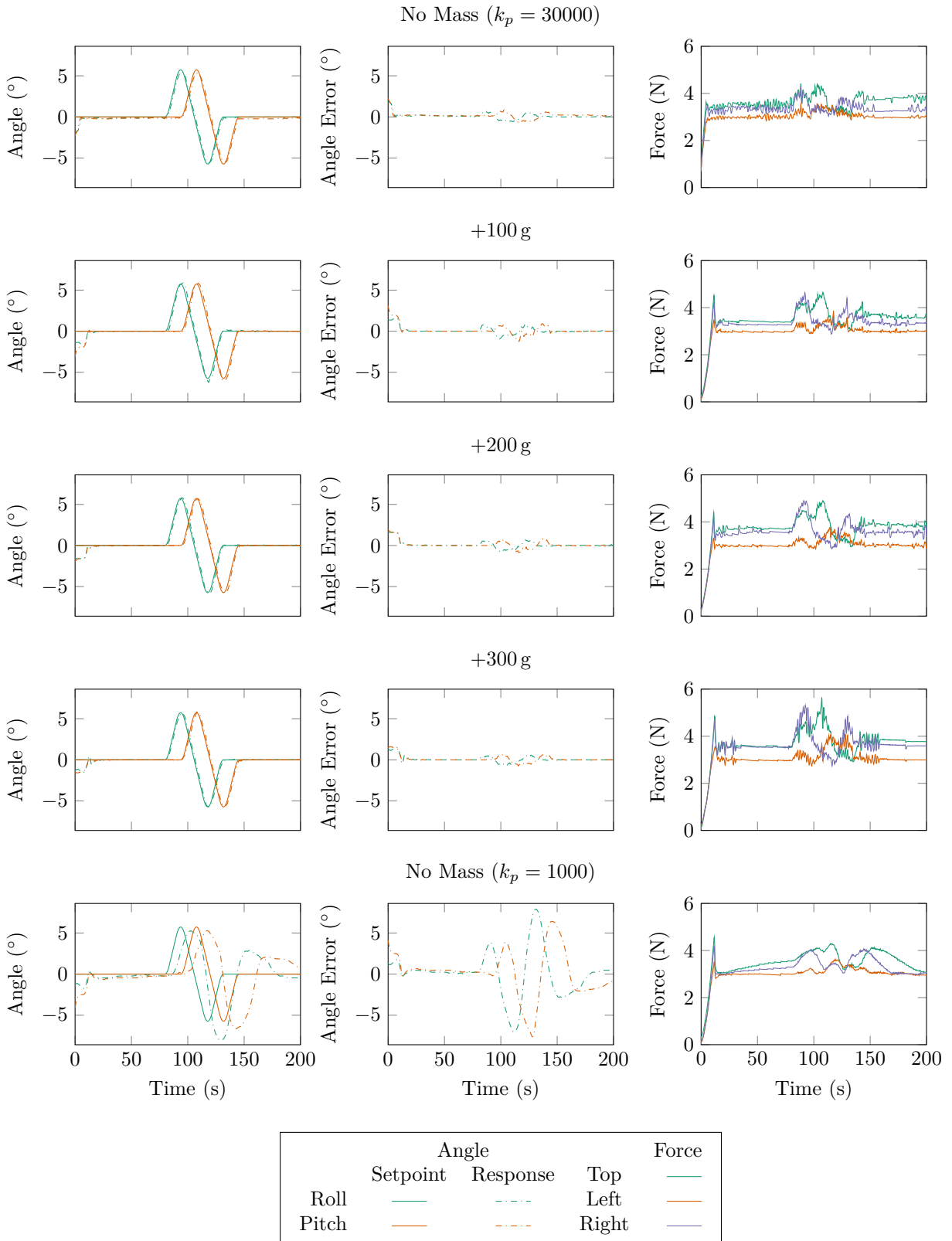


Fig. 19: AUJ pitch and roll tracking from figure 13 with increasing follower mass from table IV, as well as two different values of k_p for the “No Mass” configuration.

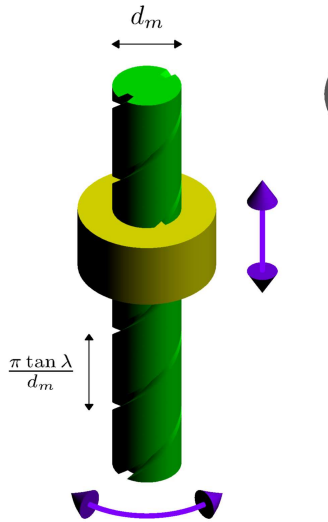


Fig. 20: Abstract diagram of a leadscrew (left) and direct drive system (right). As the screw rotates, the travelling nut moves up and down, creating a linear actuator. The direct drive employs rotary actuators to change the orientation of the AUJ directly.

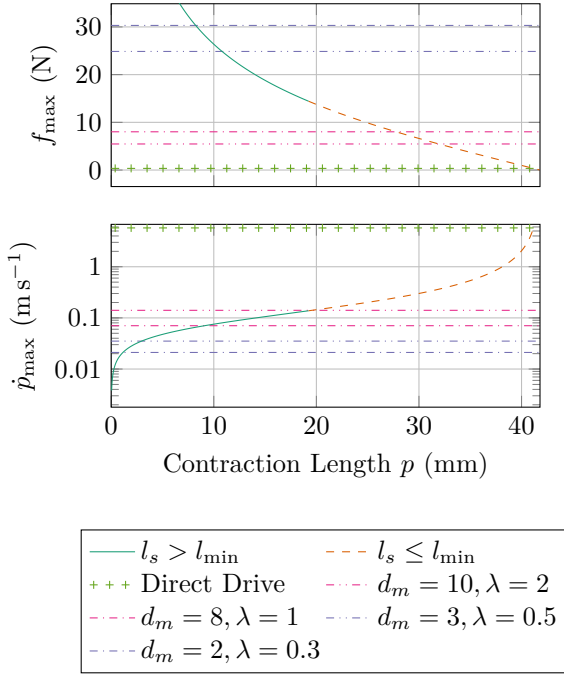
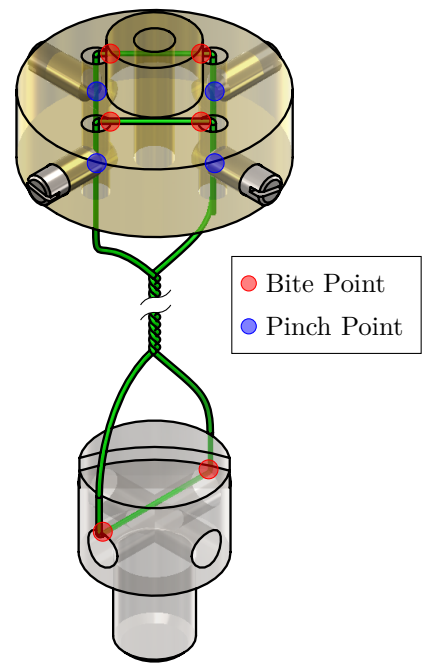


Fig. 21: Performance comparison of the TSA configuration using coefficients from table I to various leadscrew configurations with different d_m and λ , and the direct drive, where $\mu = 0.1$ for the leadscrews.

performance at low speeds, necessitating the deadband compensator. The use of similar size and torque brushless motors with sinusoidal commutation for stable low speed control could eliminate the need for the compensator, and allow for smoother AUJ motion.

Fig. 22: Cutaway of a single TSA string assembly, including the capstan and string mount, highlighting the “pinch” and “bite” points that could cause weaknesses in the string material, which may lead to premature failure.

E. Alternative Control Algorithm

Alternative control algorithms that are less or not dependant on the dynamic properties of the follower segments (mass and inertia) will also be considered, in order to improve the robustness of the control system to external forces.

F. Multiple Segments

Development of a system comprised of multiple segments is the eventual goal of the research, to demonstrate its suitability for applications such as mobile snake robots or snake-arm robots. This can use a embedded controller for each segment, controlled by a primary controller for individual joint control or inverse kinematics, as in figure 27.

VI. CONCLUSION

This research has successfully demonstrated force based control of the orientation of a universal joint using TSA in an antagonistic triad configuration, at various velocities and follower loads. It has also compared the performance of the system to alternative actuation methods, and found that its non-linear nature makes it difficult to directly compare to similar linear actuators in the same application. Finally, it has examined the limitations of the current design, and has proposed design modifications to improve range and accuracy.

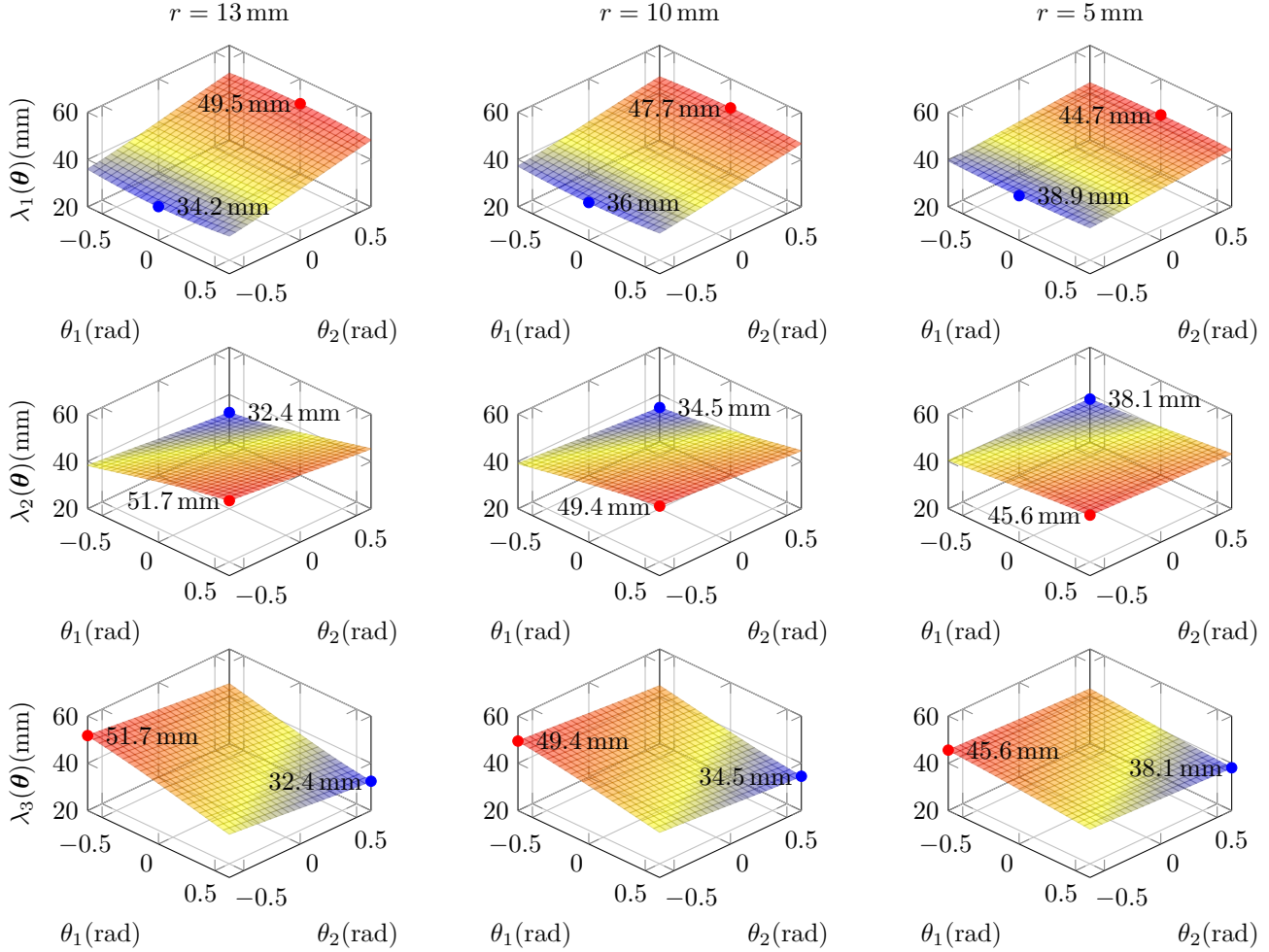


Fig. 23: Surface plots, minima and maxima for the lengths of $\lambda_{1,2,3}$ at $r = 13 \text{ mm}$, $r = 10 \text{ mm}$ and $r = 5 \text{ mm}$ in the range $[-\frac{\pi}{5}, \frac{\pi}{5}]$. As r decreases, the difference between the minima and maxima also decreases. This means that a lower value of r requires a smaller stroke range of the TSA for a given AUJ angle range.

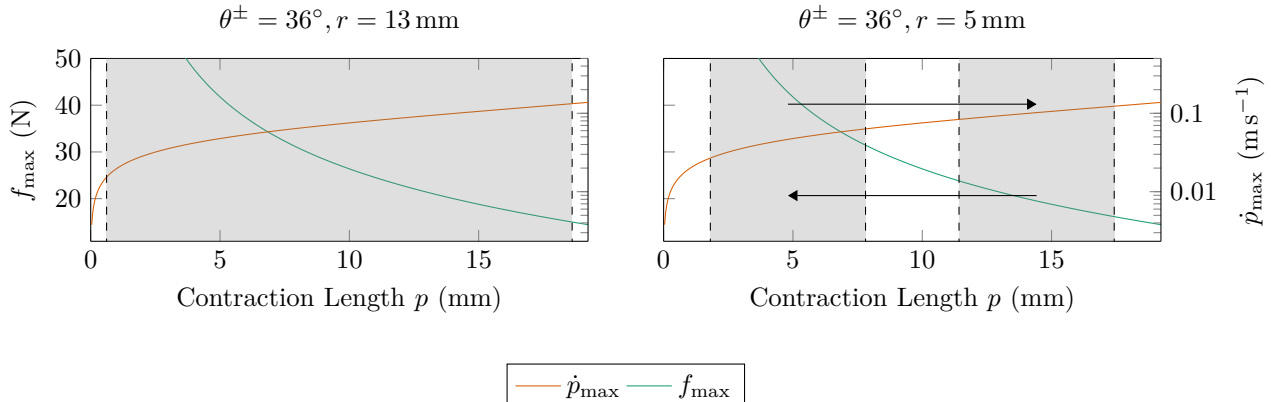


Fig. 24: By decreasing r , not only can the AUJ angle range be increased by reducing the TSA stroke range, which is marked in grey, but by adjusting f_{\min} , the transmission ratio of the TSA can be altered. Reducing f_{\min} increases the maximum TSA force f_{\max} while reducing the maximum TSA stroke velocity \dot{p}_{\max} . Conversely, increasing f_{\min} reduces f_{\max} and increases \dot{p}_{\max} . This can be used to actively modify the dynamic properties of the AUJ during operation.

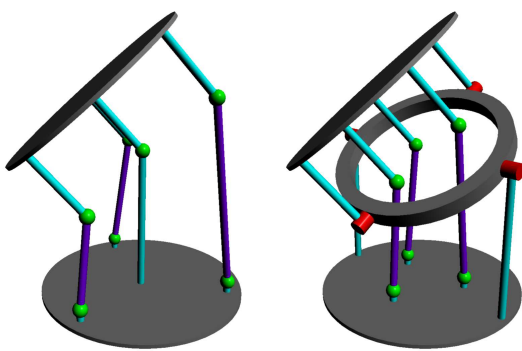


Fig. 25: An AUJ with a central universal joint, and one with a hollow spider. The hollow spider allows r to be decreased as space is no longer required for a central universal joint.

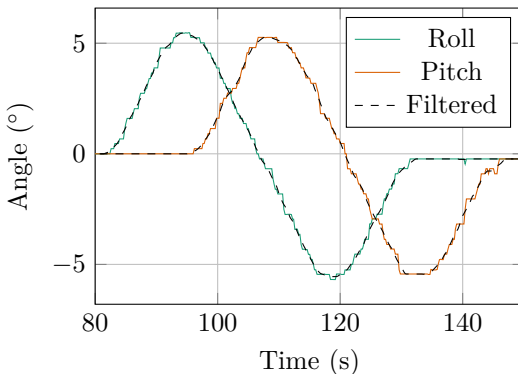


Fig. 26: Graph showing the AUJ orientation calculated from the raw IMU data, and smoothed data with the Savitsky-Golay filter applied.

VII. ACKNOWLEDGEMENT

This work was supported by a UKRI EPSRC doctoral training partnership, award reference 1957210.

REFERENCES

- [1] R. Buckingham and A. Graham, "Nuclear snake-arm robots," *Industrial Robot: An International Journal*, 2012.
- [2] M. Luo, R. Yan, Z. Wan, et al., "Orisnake: Design, fabrication, and experimental analysis of a 3-d origami snake robot," *IEEE Robotics and Automation Letters*, vol. 3, no. 3, pp. 1993–1999, 2018.
- [3] W. S. Rone, W. Saab, and P. Ben-Tzvi, "Design, Modeling, and Integration of a Flexible Universal Spatial Robotic Tail," *Journal of Mechanisms and Robotics*, vol. 10, no. 4, Apr. 2018, 041001, ISSN: 1942-4302. doi: 10.1115/1.4039500.
- [4] T. Würtz, C. May, B. Holz, C. Natale, G. Palli, and C. Melchiorri, "The twisted string actuation system: Modeling and control," in *2010 IEEE/ASME International Conference on Advanced Intelligent Mechatronics*, Jul. 2010, pp. 1215–1220. doi: 10.1109/AIM.2010.5695720.
- [5] P. Muehlbauer, M. Schimbera, K. Stewart, and P. P. Pott, "Twisted string actuation for an active modular hand orthosis," in *ACTUATOR; International Conference and Exhibition on New Actuator Systems and Applications 2021*, VDE, 2021, pp. 1–4.
- [6] J. Park, J.-i. Park, H.-T. Seo, Y. Liu, K.-S. Kim, and S. Kim, "Control of tendon-driven (twisted-string actuator) robotic joint with adaptive variable-radius pulley," in *2020 20th International Conference on Control, Automation and Systems (ICCAS)*, IEEE, 2020, pp. 1096–1098.
- [7] B. Suthar and S. Jung, "Design and feasibility analysis of a foldable robot arm for drones using a twisted string actuator: Frad-tsa," *IEEE Robotics and Automation Letters*, vol. 6, no. 3, pp. 5769–5775, 2021. doi: 10.1109/LRA.2021.3084890.
- [8] S. Nedelchev, I. Gaponov, and J. Ryu, "Accurate dynamic modeling of twisted string actuators accounting for string compliance and friction," *IEEE Robotics and Automation Letters*, vol. 5, no. 2, pp. 3438–3443, 2020. doi: 10.1109/LRA.2020.2970651.
- [9] D. Bombara, R. Konda, E. Chow, and J. Zhang, "Physics-based kinematic modeling of a twisted string actuator-driven soft robotic manipulator," in *2022 American Control Conference (ACC)*, 2022.
- [10] D. Crosby, J. Carrasco, W. Heath, and A. Weightman, "A novel triad twisted string actuator for controlling a two degrees of freedom joint: Design and experimental validation," in *2022 International Conference on Robotics and Automation (ICRA)*, IEEE, 2022, pp. 11388–11394.
- [11] M. W. Spong, S. Hutchinson, and M. Vidyasagar, *Robot modeling and control*. John Wiley & Sons, 2020.
- [12] F. Dessen, "Coordinating control of a two degrees of freedom universal joint structure driven by three servos," in *Proceedings. 1986 IEEE International Conference on Robotics and Automation*, vol. 3, Apr. 1986, pp. 817–822. doi: 10.1109/ROBOT.1986.1087559.
- [13] *Dc micromotors - precious metal commutation*, Dr. Fritz Fauhaber GmbH & Co. KG, Feb. 2020.
- [14] J. Shigley, C. Mischke, and R. Budynas, *Mechanical Engineering Design* (McGraw-Hill series in mechanical engineering). McGraw-Hill, 2004, ISBN: 9780072520361.
- [15] B. Goswami and J. Hearle, "A comparative study of nylon fiber fracture," *Textile Research Journal*, vol. 46, no. 1, pp. 55–70, 1976.
- [16] M. Toney and P. Schwartz, "Bending and torsional fatigue of nylon 66 monofilaments," *Journal of applied polymer science*, vol. 46, no. 11, pp. 2023–2032, 1992.
- [17] D. Hennessey, E. Carey, C. Simms, A. Hanly, and D. Winter, "Torsion of monofilament and polyfilament sutures under tension decreases suture strength and increases risk of suture fracture," *Journal of the Me-*

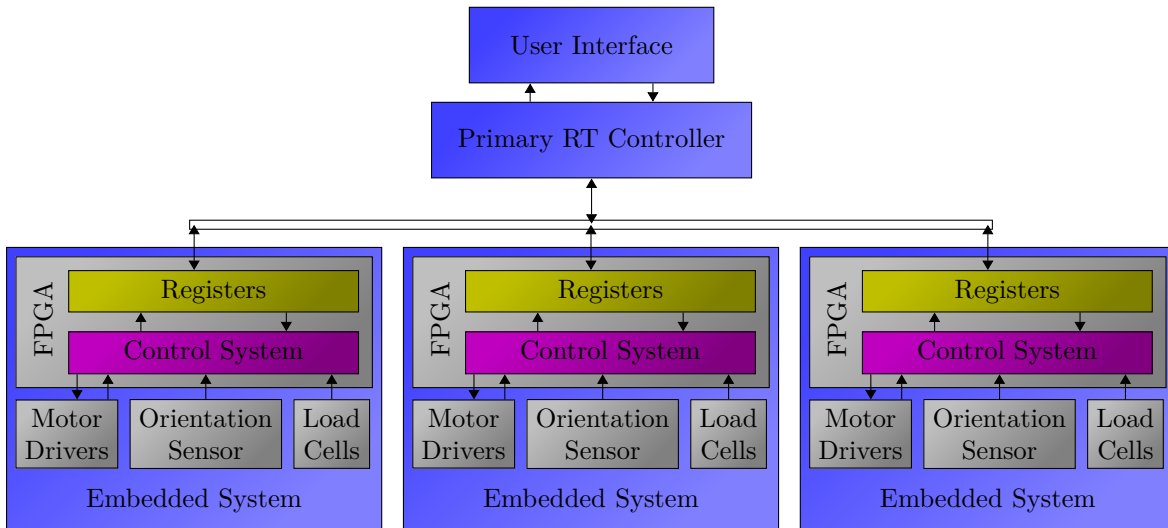


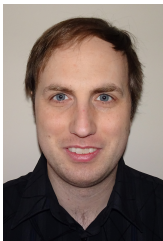
Fig. 27: Proposed system architecture for a future multi-segment system. Each segment has an embedded FPGA controller programmed with the cascaded control loop in section II. The FPGA interfaces with the load cells for each TSA, the orientation sensor for the AUJ, and the drivers for the TSA motors (the FPGA may include some motor control for a more compact design). A primary real-time controller then uses a common control bus to interface with the embedded controllers, reading and writing FPGA registers to issue motion commands and get status updates.

chanical Behavior of Biomedical Materials, vol. 12, pp. 168–173, 2012.

- [18] G. Palli, C. Natale, C. May, C. Melchiorri, and T. Wurtz, “Modeling and control of the twisted string actuation system,” *IEEE/ASME Transactions on Mechatronics*, vol. 18, no. 2, pp. 664–673, 2012.



Prof. William P. Heath is Chair of Feedback and Control in the School of Electrical and Electronic Engineering, University of Manchester, Manchester, U.K. He received the B.A. and M.A. degrees in mathematics from Cambridge University, U.K., in 1987 and 1991, and the M.Sc. and Ph.D. degrees in systems and control from the University of Manchester Institute of Science and Technology, U.K., in 1989 and 1992, respectively. He was with Lucas Automotive from 1995 to 1998 and was a Research Academic at the University of Newcastle, Australia from 1998 to 2004. His research interests include absolute stability, multiplier theory, constrained control, and system identification.



Dr. Damian J. Crosby is a PhD student in the school of Mechanical, Aerospace and Civil Engineering, University of Manchester, Manchester, U.K. He received a B.Sc. in Special Effects Development from The University of Bolton, U.K., in 2010, and a M.Res. in Robotics from The University of Plymouth, U.K., in 2012. He worked as a Research Technician at The University of Manchester from 2013 to 2017, before commencing his PhD.



Dr. Joaquin Carrasco is a Lecturer at the School of Electrical and Electronic Engineering, University of Manchester, UK. He was born in Abaran, Spain, in 1978. He received the B.Sc. degree in physics and the Ph.D. degree in control engineering from the University of Murcia, Murcia, Spain, in 2004 and 2009, respectively. From 2009 to 2010, he was with the Institute of Measurement and Automatic Control, Leibniz Universitt Hannover, Hannover, Germany. From 2010 to 2011, he was a research associate at the Control Systems Centre, School of Electrical and Electronic Engineering, University of Manchester, UK.



Prof. Andrew Weightman graduated in 2006 with a PhD in Mechanical Engineering from the University of Leeds. Whilst at the University of Leeds he developed rehabilitation robotic technology for improving upper limb function in adults and children with neurological impairment which was successfully utilised in homes, schools and clinical settings. In 2013 he moved to the University of Manchester, School of Mechanical, Aerospace and Civil Engineering as a Lecturer in Medical Mechatronics. Prof. Weightman has research interests in biomimetic mobile robotics, rehabilitation robotics, robotics for nuclear decommissioning and collaborative robotics.